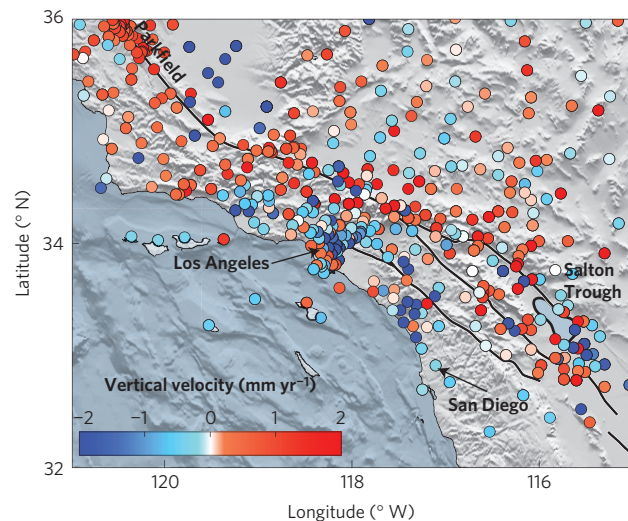


# The vertical fingerprint of earthquake cycle loading in southern California

Samuel Howell<sup>1\*</sup>, Bridget Smith-Konter<sup>1</sup>, Neil Frazer<sup>1</sup>, Xiaopeng Tong<sup>2</sup> and David Sandwell<sup>3</sup>

**The San Andreas Fault System, one of the best-studied transform plate boundaries on Earth, is well known for its complex network of locked faults that slowly deform the crust in response to large-scale plate motions<sup>1–8</sup>. Horizontal interseismic motions of the fault system are largely predictable, but vertical motions arising from tectonic sources remain enigmatic. Here we show that when carefully treated for spatial consistency, global positioning system-derived vertical velocities expose a small-amplitude ( $\pm 2 \text{ mm yr}^{-1}$ ), but spatially considerable (200 km), coherent pattern of uplift and subsidence straddling the fault system in southern California. We employ the statistical method of model selection to isolate this vertical velocity field from non-tectonic signals that induce velocity variations in both magnitude and direction across small distances (less than tens of kilometres; ref. 9), and find remarkable agreement with the sense of vertical motions predicted by physical earthquake cycle models spanning the past few centuries<sup>6,10</sup>. We suggest that these motions reveal the subtle, but identifiable, tectonic fingerprint of far-field flexure due to more than 300 years of fault locking and creeping depth variability. Understanding this critical component of interseismic deformation at a complex strike-slip plate boundary will better constrain regional mechanics and crustal rheology, improving the quantification of seismic hazards in southern California and beyond.**

Crustal motions surrounding the San Andreas Fault System (SAFS) in southern California are densely sampled by EarthScope's Plate Boundary Observatory (PBO) global positioning system (GPS) array, providing high-quality, well-behaved horizontal surface velocity solutions spanning a major and active transform plate boundary. When imposed as boundary conditions on physical models of deformation throughout the earthquake cycle (interseismic strain accumulation, coseismic displacement, and postseismic relaxation), these velocity measurements can be used to constrain the faulting characteristics of the SAFS (for example, slip rates, fault locking depths<sup>6,11</sup>) and lithospheric rheology (for example, crust/mantle viscosities and thicknesses<sup>2,4–6,12</sup>). Whereas vertical deformation from earthquake cycle loading is a measurable process at subduction zone plate boundaries, where steady interseismic motion is augmented by step displacements during an earthquake<sup>13,14</sup>, vertical deformation at transform plate boundaries is much more challenging to detect<sup>4</sup>. Unlike the smooth, predictable crustal motions exhibited by the horizontal velocity field, PBO vertical velocity data are typically dominated by short-wavelength (<10s km), non-tectonic signals that potentially mask underlying long-wavelength tectonic deformation (Fig. 1). Recently, several high-profile studies have used vertical velocity



**Figure 1 | Southern California vertical GPS velocity data.** Unfiltered vertical EarthScope PBO GPS velocities in southern California, revealing sporadic variation over distances of tens of kilometres, attributed to non-tectonic signals.

measurements to investigate groundwater storage and depletion in California<sup>15–17</sup>. However, no such study has investigated the large-scale tectonic component of vertical rates along the SAFS, which we suggest contains a dominant and smoothly varying signal from earthquake cycle loading.

To inspect the vertical motions associated with the SAFS earthquake cycle, we used published EarthScope PBO GPS vertical velocity estimates (epoch year 2014<sup>18</sup>). We first omitted GPS stations that were likely to have been affected by non-tectonic sources of deformation, based on anomalies revealed by high-resolution interferometric synthetic aperture radar (InSAR) data<sup>7</sup>, as well as stations with velocities  $>5 \text{ mm yr}^{-1}$  and low signal-to-noise ratios ( $\leq 5:1$ ). We then processed the remaining stations into a local reference frame ( $115^{\circ}$ – $121^{\circ}$  W,  $32^{\circ}$ – $36^{\circ}$  N) by removing the mean velocity of the remaining stations. Vertical GPS measurements are known to be sensitive to a variety of factors (such as variations in GPS monument type and stability, monument substrate material, local surface geology, proximity to reflectors, ionospheric and tropospheric signal delays, satellite orbits, and response to local changes in water storage, pore pressure, precipitation, and water runoff), all of which can introduce complex and widely varying vertical signals<sup>9</sup>.

<sup>1</sup>Department of Geology and Geophysics, SOEST, University of Hawai'i at Manoa, Honolulu, Hawaii 96822, USA. <sup>2</sup>Department of Earth and Space Sciences, University of Washington, Seattle, Washington 98195, USA. <sup>3</sup>Scripps Institute of Oceanography, University of California San Diego, San Diego, California 92093, USA. \*e-mail: [howellsm@hawaii.edu](mailto:howellsm@hawaii.edu)

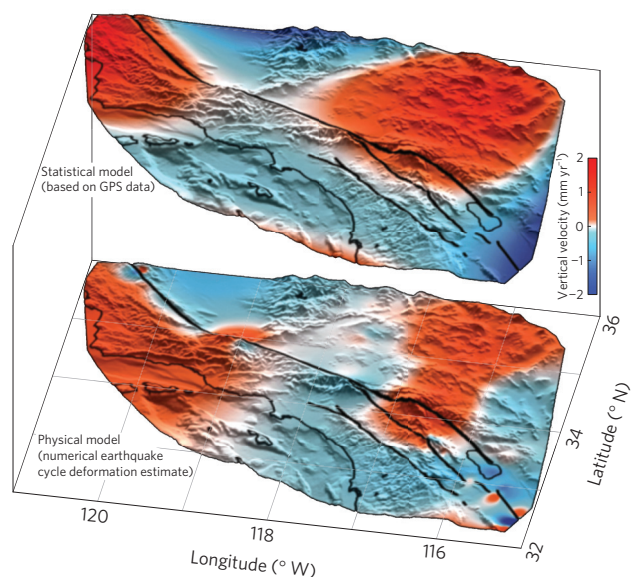


**Figure 2 | GPS and physical model comparison.** Vertical velocities predicted by model selection (statistical, s-model) using GPS data and the best-fitting physical deformation model (p-model) simulating the vertical crustal response of earthquake cycle loading at depth throughout the past 300 or more years. The p-model velocity estimate represents regional vertical motion due to the interaction of creeping and locked faults embedded within a 50-km-thick elastic plate overlaying an asthenosphere with a viscosity of  $1 \times 10^{19}$  Pa s. Vertical velocity estimates overlaying shaded topographic relief are saturated near  $\pm 1.5$  mm yr $^{-1}$  to highlight agreement in the sense of motion between data and model predictions.

As non-tectonic signals appear to dominate the first-order vertical velocity field of the SAFS, we employed the statistical method of model selection<sup>19</sup> to carefully distinguish more subtle long-wavelength signals that could be of tectonic origin. Model selection provides an objective estimate of the velocity field that optimizes goodness of fit while penalizing model complexity, as measured by the number of model terms<sup>19,20</sup>. We inverted the velocity data to obtain phenomenological statistical model (s-model) surfaces of increasing complexity that minimized the sum of squared residuals of the data and the s-model on a 1-km-spaced grid spanning the  $560 \times 440$  km study area. As the complexity of the s-model increased, the fit necessarily improved, and so did the likelihood of overfitting the dominant short-spatial-scale variations. Thus, the sample-size-corrected Akaike Information Criterion was used to select the point at which increasing the number of model terms did not improve the fit sufficiently to warrant a higher-order model<sup>20</sup>. The resultant s-model contains 15 terms (additional details of the statistical analysis are included in the Methods, and velocity estimates at multiple orders are shown in the Supplementary Information). This optimal s-model (Fig. 2) reveals a distinct, smoothly varying quadrant pattern of uplift and subsidence in the southern California vertical velocity field, while excluding the higher-order signals which dominate the visual scatter of the data. The northwest and east quadrants of the s-model show  $\sim 200$  km diameter ‘lobes’ of uplift (maximum 1.9, median 0.6 mm yr $^{-1}$ ), whereas the north and southwest quadrants reveal similar-sized lobes of subsidence (minimum  $-2.1$ , median  $-0.4$  mm yr $^{-1}$ ). Smaller amplitude, shorter-wavelength postseismic deformation following the 1992 M7.3 Landers and 1999 M7.1 Hector Mine earthquakes may also influence the solution obtained with higher-order models, but these local patterns are smoothed into the broader regional pattern at the preferred model order. Because results obtained with this approach can be mildly affected by model

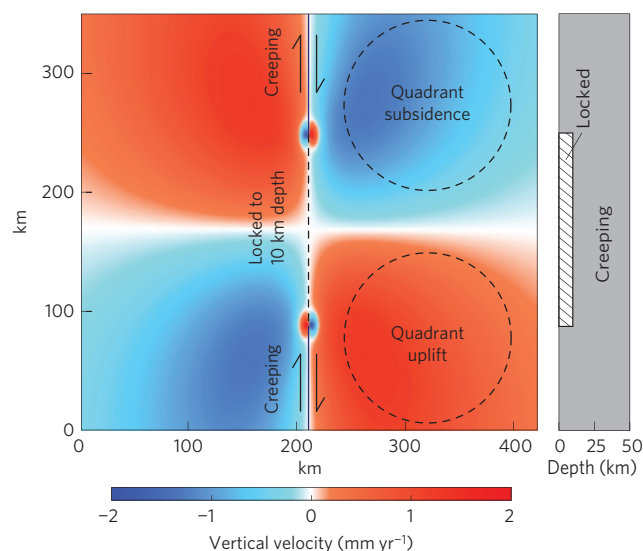


**Figure 3 | Simplified physical model vertical velocity pattern.** Left: map view representation of interseismic quadrant lobe patterns of vertical motion from bending moments induced by variations in fault locking (or creeping) depth. Right: cross-section view of fault geometry. Here a centrally locked fault extends from the surface to 10 km depth and is embedded within a 50-km-thick elastic plate overlaying an asthenosphere with a viscosity of  $1 \times 10^{19}$  Pa s. The fault is surrounded by top-to-bottom creeping zones to the north and south.

order, these results were also verified independently using splining techniques<sup>21,22</sup> (see Methods).

Although this clear quadrant pattern of vertical motions straddling the SAFS may seem perplexing, similar, but smaller-scale, patterns of uplift and subsidence have been observed for large strike-slip earthquakes as a result of coseismic fault slip and post-seismic viscoelastic relaxation<sup>1-4,23</sup>. Likewise, interseismic strain accumulation at depth can generate long-wavelength, low-magnitude quadrant lobe patterns in vertical velocity that arise from a major transition in locking-creeping depth<sup>6,10</sup> (Fig. 3). Along the SAFS, variations in fault locking depth, constrained by horizontal GPS and InSAR data<sup>6,11</sup>, are well documented, extending from the Salton Trough to Parkfield, where the upper  $\sim 10$ – $15$  km of the fault has remained locked since at least the 1857 M7.9 Fort Tejon rupture (Fig. 4). Critical to this study, however, are the major sections of fault creep bounding this locked zone: the ‘Creeping’ segment north of Parkfield<sup>24</sup> and shallow creep accommodated by the collection of faults that bound the southern edge of the Salton Trough (Superstition Hills, Brawley, Imperial, and Cerro Prieto segments)<sup>25</sup>.

Using a semi-analytic physical model (p-model) representing three-dimensional (3D) elastic-viscoelastic earthquake cycle deformation<sup>6,10</sup> that includes the restoring force of gravity<sup>26</sup> (see Methods), we calculated the present-day vertical velocity field from an a priori inversion of horizontal PBO velocity data<sup>11</sup>. Interseismic deep slip below locked fault patches generates the first-order orientation and magnitude of this velocity field, whereas second-order effects arise from local slip-rate variability, earthquake cycle viscoelastic relaxation, and abrupt changes in fault locking depth (Figs 2 and 3 and Supplementary Fig. 3). Hence the p-model shows two large lobes of uplift (maximum 0.9, median 0.3 mm yr $^{-1}$ ) and subsidence (minimum  $-0.7$ , median  $-0.2$  mm yr $^{-1}$ ) in response to the interseismic loading history of the SAFS. The geometry of the p-model vertical velocity lobes varies with assumed lithospheric thickness, whereas the magnitude of uplift and subsidence varies with asthenospheric viscosity and prescribed fault locking depth (see Supplementary Information). If another significant event

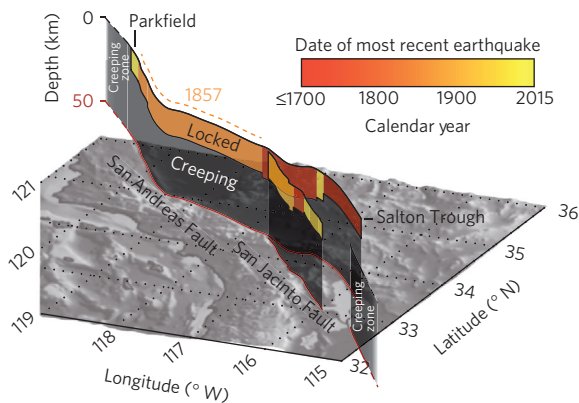


**Figure 4 | Simplified schematic of SAFS locking depth variations and historical earthquake sequence.** Locked SAFS segments are represented in colour to illustrate the historical earthquake sequence. Creeping and partially creeping (south of the Salton Trough) sections of the fault are shown in grey. Segments from Parkfield to the Salton Trough have been locked since at least the M7.9 1857 Fort Tejon earthquake, whereas segments bounding this region accommodate strain primarily through aseismic creep.

like the 1857 rupture occurs, the moment will extinguish and the vertical lobate pattern will relax over the Maxwell timescale<sup>10</sup>.

The first-order vertical velocity trends predicted by the p-model are remarkably consistent with those preferred by the GPS-derived s-model. Quantitative comparisons (mean residual, ratio of uplift and subsidence medians, and alignment) of the s-model with a suite of different p-model rheologies (elastic plate thicknesses of 30–70 km and asthenospheric viscosities of  $3 \times 10^{18}$ – $3 \times 10^{19}$  Pa s) provide critical insight into the overall agreement between model and data (see Supplementary Information). The alignment was calculated as the fraction of the study region where both the s-model and p-model predicted the same direction of vertical motion. We found that the residual norm is minimized and the alignment maximized for a p-model with a 50-km-thick lithosphere overlying a  $1 \times 10^{19}$  Pa s asthenosphere (Fig. 2), consistent with previous work<sup>6,8,11</sup>. We also found that the p-model underpredicted median uplift and subsidence by greater than a factor of two compared to the s-model. The source of this difference is not well resolved, although it may be partially attributed to an overestimation of elastic plate thickness; a thinner elastic plate will yield higher velocity amplitudes at the expense of a smaller-wavelength deformation pattern.

It is remarkable that the physical (p-) earthquake cycle models, constrained using only horizontal interseismic GPS measurements, accurately predict the appropriate sense, relative magnitude, and spatial pattern of far-field vertical velocity variations exhibited by the optimal statistical (s-) model. Such agreement has several important implications. First, vertical GPS observations, although noisy by nature, are capable of documenting elastic plate flexure caused by bending moments applied at the ends of locked sections of faults. Lateral variations in vertical velocities of such extent may have significant bearing on studies of glacial melting and sea-level change<sup>27,28</sup>. Second, the agreement between data and models suggests that the earthquake cycle loading process, including the role of gravity-induced plate flexure and fault locking depth variability, is sufficiently well understood to predict complex patterns of vertical deformation. Third, recent studies of vertical GPS velocities in California largely attribute long-wavelength uplift and subsidence signals to the isostatic response of the crust to changes in the storage and discharge of groundwater<sup>15–17</sup>. These studies have been critical to advancing our understanding of groundwater use and replenishment, and the extent of the ongoing

historic drought affecting the region. However, elastic models of crustal rebound due to San Joaquin water extraction, for example, have underpredicted vertical GPS velocities in some regions by almost  $2 \text{ mm yr}^{-1}$ , leaving open the possibility of a time-dependent tectonic contribution<sup>15</sup>. Given the contribution of vertical motions from the historical earthquake cycle demonstrated in this study, the dominant sources of vertical deformation in California are probably a combination of long-wavelength groundwater-induced isostasy and regional earthquake cycle strain of the many active faults within the SAFS. Finally, the current GPS array is ideally situated to map and model the large-scale time-dependent relaxation of the mantle resulting from the next significant rupture of the SAFS. These results have implications for seismic moment deficit<sup>29</sup> and seismic hazard mitigation of active faults in southern California.

## Methods

Methods, including statements of data availability and any associated accession codes and references, are available in the [online version of this paper](#).

Received 5 September 2015; accepted 18 May 2016; published online 20 June 2016

## References

- Massonnet, D. *et al.* The displacement field of the Landers earthquake mapped by radar interferometry. *Nature* **364**, 138–142 (1993).
- Deng, J., Gurnis, M., Kanamori, H. & Hauksson, E. Viscoelastic flow in the lower crust after the 1992 Landers, California, earthquake. *Science* **282**, 1689–1692 (1998).
- Fialko, Y., Simons, M. & Agnew, D. The complete (3-D) surface displacement field in the epicentral area of the 1999  $M_w$ 7.1 Hector Mine earthquake, California, from space geodetic observations. *Geophys. Res. Lett.* **28**, 3063–3066 (2001).
- Pollitz, F. F., Wicks, C. & Thatcher, W. Mantle flow beneath a continental strike-slip fault: postseismic deformation after the 1999 Hector Mine earthquake. *Science* **293**, 1814–1818 (2001).
- Johnson, K. M. & Segall, P. Viscoelastic earthquake cycle models with deep stress-driven creep along the San Andreas Fault System. *J. Geophys. Res.* **109**, B10403 (2004).
- Smith-Konter, B. & Sandwell, D. T. A model of the earthquake cycle along the San Andreas Fault System for the past 1000 years. *J. Geophys. Res.* **111**, B01405 (2006).
- Tong, X., Sandwell, D. T. & Smith-Konter, B. High-resolution interseismic velocity data along the San Andreas Fault from GPS and InSAR. *J. Geophys. Res.* **118**, 369–389 (2013).
- Smith-Konter, B. R., Thornton, G. M. & Sandwell, D. T. Vertical crustal displacement due to interseismic deformation along the San Andreas Fault: constraints from tide gauges. *Geophys. Res. Lett.* **41**, 3793–3801 (2014).
- Blume, F. *et al.* *Stability of GNSS Monumentation: Analysis of Co-Located Monuments in the Plate Boundary Observatory Fall Meeting 9–13 December*, abstract number G51B-04 (American Geophysical Union, 2013).
- Smith, B. & Sandwell, D. T. A 3-D semi-analytic viscoelastic model for time-dependent analyses of the earthquake cycle. *J. Geophys. Res.* **109**, B12401 (2004).
- Tong, X., Smith-Konter, B. & Sandwell, D. T. Is there a discrepancy between geological and geodetic slip rates along the San Andreas Fault System? *J. Geophys. Res.* **119**, 2518–2538 (2014).
- Hetland, E. A. & Hager, B. H. Postseismic and interseismic displacements near a strike-slip fault: a two-dimensional theory for general linear viscoelastic rheologies. *J. Geophys. Res.* **110**, B10401 (2005).
- Melini, D. *et al.* Earthquakes and relative sea level changes. *Geophys. Res. Lett.* **31**, L09601 (2004).
- Sieh, K. *et al.* Earthquake supercycles inferred from sea-level changes recorded in the corals of West Sumatra. *Science* **322**, 1674–1678 (2008).
- Amos, C. B. *et al.* Uplift and seismicity driven by groundwater depletion in central California. *Nature* **509**, 483–486 (2014).
- Argus, D. F., Fu, Y. & Landerer, F. W. Seasonal variation in total water storage in California inferred from GPS observations of vertical land motion. *Geophys. Res. Lett.* **41**, 1971–1980 (2014).
- Borsa, A. A., Agnew, D. C. & Cayan, D. R. Ongoing drought-induced uplift in the western United States. *Science* **345**, 1587–1590 (2014).
- EarthScope Plate Boundary Observatory* (UNAVCO, accessed January 2015); <http://pbo.unavco.org/data/gps>

19. Burnham, K. P. & Anderson, D. R. *Model Selection and Multimodel Inference: A Practical Information-Theoretic Approach* 2nd edn (Springer, 2002).
20. Burnham, K. P. & Anderson, D. R. Multimodel inference: understanding AIC and BIC in model selection. *Sociol. Methods Res.* **33**, 261–304 (2004).
21. MATLAB *Statistics Toolbox Release 2014b* (The MathWorks, 2014).
22. Wessel, P. A general-purpose Green's function-based interpolator. *Comput. Geosci.* **35**, 1247–1254 (2009).
23. Freed, A. M. & Burgmann, R. Evidence of power-law flow in the Mojave Desert mantle. *Nature* **430**, 548–551 (2004).
24. Moore, D. E. & Rymer, M. J. Talc-bearing serpentinite and the creeping section of the San Andreas Fault. *Nature* **448**, 795–797 (2007).
25. Lyons, S. N., Bock, Y. & Sandwell, D. T. Creep along the Imperial Fault, southern California, from GPS measurements. *J. Geophys. Res.* **107**, 2249 (2002).
26. Sandwell, D. T. *et al.* *Investigations into Effects of Different Modeling Codes and Rheology on Predicted Coseismic and Postseismic Surface Deformation* Annual Meeting 8–12 September, Tectonic Geodesy Poster 239 (Southern California Earthquake Center, 2012).
27. Conrad, C. P. The solid Earth's influence on sea level. *Geol. Soc. Am. Bull.* **125**, 1027–1052 (2013).
28. Peltier, W. R. Global sea level rise and glacial isostatic adjustment. *Glob. Planet. Change* **20**, 93–12 (1999).
29. Tong, X., Sandwell, D. & Smith-Konter, B. An integral method to estimating the moment accumulation rate on the creeping section of the San Andreas Fault. *Geophys. J. Int.* **203**, 48–62 (2015).

## Acknowledgements

We thank P. Wessel and J. Foster for their preliminary review of this manuscript, J. Foster for clarifying sources of data noise, and G. Thornton for his initial modelling efforts that contributed to this work. This study was supported by National Science Foundation grants EAR-0838252 and EAR-1424374. This material is based on data provided by the Plate Boundary Observatory operated by UNAVCO for EarthScope ([www.earthscope.org](http://www.earthscope.org)) and supported by the National Science Foundation No. EAR-0350028 and EAR-0732947.

## Author contributions

S.H. performed the statistical GPS data analysis and comparisons between statistical and physical models, prepared figures, and wrote the paper. B.S.-K. produced vertical velocity field for physical numerical models. N.F. offered guidance on the statistical methods. B.S.-K. and X.T. identified spurious GPS data using InSAR. D.S. offered guidance on regional geology and deformation, as well as the scope and presentation of the study. All authors discussed the study results and improved the manuscript.

## Additional information

Supplementary information is available in the [online version of the paper](#). Reprints and permissions information is available online at [www.nature.com/reprints](http://www.nature.com/reprints). Correspondence and requests for materials should be addressed to S.H.

## Competing financial interests

The authors declare no competing financial interests.

Methods

**Statistical analysis of GPS vertical velocities.** The premise of this study relies on nested models of the form

$$d(x, y) = \beta_0 + \beta_1 x + \beta_2 y + \beta_3 xy + \beta_4 x^2 + \beta_5 y^2 + \beta_6 x^2 y + \beta_7 xy^2 + \dots + \varepsilon \tag{1}$$

where the data vector,  $\mathbf{d}$ , is the GPS measured vertical velocity at location  $(x, y)$ ,  $\beta_m$  are the least-squares polynomial coefficients to invert for, and  $\varepsilon$  characterizes the data noise about the modelled surface. The model order,  $l$ , is the sum of the exponents of the highest-order term. For example, the model ending with the term  $xy^2$  is considered to be order  $l = 3$ . For increasing model order, cross-terms are added first, then terms with higher powers of  $x$  than  $y$ , and finally those with higher powers of  $y$  than  $x$ . The terms for model order  $l = 2$  would thus be arranged  $\beta_3 xy + \beta_4 x^2 + \beta_5 y^2$  as above.

We begin with the linear equation

$$\mathbf{d} = \mathbf{G}\mathbf{m} + \boldsymbol{\varepsilon} \tag{2}$$

where  $\mathbf{G}$  is the design matrix, with columns comprised of the independent terms  $(x_n, y_n)$  in equation (1), and  $\mathbf{m}$  is a vector of polynomial coefficients  $\beta_m$ .

$$\begin{bmatrix} d_1 \\ d_2 \\ d_3 \\ \vdots \\ d_N \end{bmatrix} = \begin{bmatrix} 1 & x_1 & y_1 & x_1 y_1 & x_1^2 & \dots \\ 1 & x_2 & y_2 & x_2 y_2 & x_2^2 & \dots \\ 1 & x_3 & y_3 & x_3 y_3 & x_3^2 & \dots \\ \vdots & \vdots & \vdots & \vdots & \vdots & \ddots \\ 1 & x_N & y_N & x_N y_N & x_N^2 & \dots \end{bmatrix} \begin{bmatrix} \beta_1 \\ \beta_2 \\ \beta_3 \\ \vdots \\ \beta_M \end{bmatrix} + \boldsymbol{\varepsilon} \tag{3}$$

Here,  $\mathbf{G}$  is  $N \times M$ , where  $N$  is the number of GPS data in  $\mathbf{d}$ , and  $M$  is the number of coefficients being solved for. Before building the design matrix, the latitude and longitude of each data point were converted to UTM zone 11S easting ( $x$ ) and northing ( $y$ ) to provide an isotropic Cartesian coordinate system. The coordinate positions then had their mean removed and were scaled to unit variance to ensure stability of the inversion. We repeated this process with a rotation of the design matrix into a coordinate system that minimized areas of the modelled region with no data (white space) to ensure that the results were not affected by artefacts of the grid orientation. After building the design matrix, equation (2) was inverted for the least-squares solution of  $\mathbf{m}$

$$\mathbf{m} = (\mathbf{G}^T \mathbf{G})^{-1} \mathbf{G}^T \mathbf{d} \tag{4}$$

This inversion was performed for  $K = 2$  to 751 (through polynomial orders up to  $l = 38$ ), where  $K$  is the number of parameters used in the model,  $M$ , plus one (we independently estimated data noise from the inversion). The criterion for model selection used in this study was the sample-size-corrected Akaike Information Criterion,  $AIC_c^{19,20,30}$ ,

$$AIC_c = N \ln(RSS/N) + 2KN/(N - K - 1) \tag{5}$$

in which  $RSS$  is the residual sum of squared prediction errors. The first term in the  $AIC_c$  penalizes models that fit poorly, as measured by high  $RSS/N$ , whereas the second term penalizes model complexity, as measured by high  $K$ . Minimizing the  $AIC_c$  then yields the  $s$ -model that best fits, but does not overfit, the data; it is the simplest model that explains the correlated velocity field.

The variance of the sampling distribution (signal noise) was estimated using the explained sum of squares<sup>31</sup>,  $ESS$ ,

$$ESS = (N - K)^{-1} (\mathbf{G}\mathbf{m} - \mathbf{d})^T (\mathbf{G}\mathbf{m} - \mathbf{d}) \tag{6}$$

To produce an  $s$ -model surface and surface of standard deviation calculated on an evenly spaced UTM grid that spans the region containing the GPS data, we first calculate the covariance matrix,  $C_m$ , of the posterior distribution of parameters:

$$C_m = (\mathbf{G}^T C_n^{-1} \mathbf{G})^{-1} \tag{7}$$

Here  $C_n$  is the covariance of the signal noise,  $ESS I_N$ . We then constructed a 1 km spaced UTM grid that spans the study area to populate a new design matrix,  $\mathbf{G}'$ , at  $N'$  locations, and calculated the selected model vertical velocities,  $\mathbf{d}'$ , on the grid, as well as the covariance of the  $s$ -model prediction,  $C_{d'}$ ,

$$\mathbf{d}' = \mathbf{G}'\mathbf{m} + \boldsymbol{\varepsilon}' \tag{8}$$

$$C_{d'} = \mathbf{G}'^T C_m \mathbf{G}' + C_{\varepsilon'}$$

in which  $C_{\varepsilon'} = ESS I_{N'}$ .

At every grid location, we computed one standard deviation in the prediction of GPS velocities from the predicted model surface using the prediction covariance. Grid coordinates were fed as  $x, y$  pairs into the design matrix,  $\mathbf{G}'$ , at locations where we predicted the coherent velocity field values,  $\mathbf{d}'$ . The easting and northing positions were then scaled back to their true mean and variance before being converted to latitude and longitude. Results of this statistical technique for example model orders are provided in Supplementary Fig. 1.

We tested the sensitivity of this method to short-wavelength vertical velocity signals using synthetic data. We interpolated 5 mm  $\text{yr}^{-1}$  squares of increasing edge length (10 km–100 km) at the centre of the model domain to the GPS station locations and performed model selection on nested polynomials. The approach consistently selected high-order polynomial models that fit the square vertical velocity anomalies. When modelling the synthetic data using only the long-wavelength polynomial chosen for the GPS data used in this study (15th order), features smaller than the  $\sim 100$ –200 km wavelength of the model were smeared into broad, low-amplitude signals that would have a negligible effect on the overall solution. For example, a 50  $\times$  50 km square of 5 mm  $\text{yr}^{-1}$  is averaged into a  $\sim 150 \times 200$  km region of uplift with an amplitude of 0.4 mm  $\text{yr}^{-1}$ .

For independent verification of these modelling results, we also used Generic Mapping Tools (GMT) two-dimensional (2D) Green's function spline function 'greenspline'<sup>22</sup>, as well as the thin-plate splining function 'tpaps' in MATLAB 2014b<sup>21</sup>. Both techniques provided qualitative and quantitative verification of the long-wavelength quadrant pattern revealed by model selection (see Supplementary Fig. 1). GMT's greenspline tool for continuous curvature splines and MATLAB's tpaps tool for thin-plate splines produce a smoothed data surface that lies between the two extremes where the model output is equal to the model input and where the model output has zero curvature. Although these functions do not use a robust information criterion, the smoothing value chosen is a relatively good starting guess for the value that optimizes goodness of fit while best penalizing high spline curvature.

**3D earthquake cycle deformation model.** We model the North American–Pacific plate boundary as a series of vertical connected faults embedded in an elastic plate overlying a viscoelastic half-space<sup>6</sup>. The 4D model simulates interseismic strain accumulation, coseismic displacement, and postseismic viscous relaxation of the mantle. The mathematical deformation solution is analytic in the vertical and time dimensions, whereas the solution in the two horizontal dimensions is provided in the Fourier transform domain<sup>10,32,33</sup>. The solution satisfies the zero-traction surface boundary condition<sup>34–37</sup> and maintains stress and displacement continuity across the base of the plate<sup>10</sup>. A far-field velocity step across the plate boundary of 45 mm  $\text{yr}^{-1}$  is simulated using a cosine transform in the  $x$  direction (that is, across the plate boundary). A uniform far-field velocity boundary condition at the top and bottom of the grid is simulated by arranging the fault trace to be cyclic in the  $y$  direction (that is, parallel to the plate boundary). The numerical aspects of this approach involve generating a grid of vector force couples that simulate complex fault geometry, taking the 2D horizontal Fourier transform of the grid, multiplying by the appropriate transfer functions and time-dependent relaxation coefficients, and finally inverse Fourier transforming to obtain the desired results<sup>10</sup>. Fault elements are embedded in an elastic plate and a displacement discontinuity across each fault element is simulated using a finite width force couple embedded in a fine grid<sup>10</sup>. Because the computational aspects of the model are only 2D, the entire plate boundary (2,048 km by 1,024 km, 1 km cell size) can be simulated very efficiently.

Faults within the elastic plate extend from the surface to a prescribed locking depth. Below this, fully relaxed secular slip (assuming infinite time) takes place down to the base of the elastic plate. Assumed quantities of the homogeneous elastic plate are a Young's modulus of 70 GPa and a shear modulus of 30 GPa (refs 6,38). Coseismic slip is kinematically prescribed along fault segments with known historical ruptures. Transient deformation follows each earthquake due to viscoelastic flow in the underlying half-space. The duration of the viscoelastic response, characterized by the Maxwell time, depends on the viscosity of the underlying half-space and the elastic plate thickness (see Supplementary Fig. 2 for model parameter comparison). The Maxwell rheology used is consistent with viscoelastic postseismic studies of southern California<sup>39–42</sup>. Full details of this model are provided in previous studies<sup>6,10</sup>.

The model is purely kinematic; slip on faults is prescribed based on geologic, geodetic, and historical seismic data. Deep slip along the plate boundary (below the locking depth) drives the secular interseismic crustal block motions. Long-term slip rates (that is, over many earthquake cycles) are constrained by geologic estimates<sup>43</sup> and geodetic velocity measurements<sup>11</sup>. Small adjustments to local fault geometry to account for fault step-overs<sup>7</sup> were adopted in the present-day velocity model (Supplementary Fig. 3). Fault segments were locked from the surface down to a variable locking depth, which was tuned to match the present-day EarthScope PBO GPS measurements<sup>11</sup>. Note that earthquake cycle effects<sup>44,45</sup>, as well as a smooth transition from locked to unlocked fault<sup>46</sup>, are known to complicate estimations of true locking depth. Apparent locking depths range between 0 and 22 km, and are primarily consistent with seismicity depths<sup>47,48</sup> and provide a root-mean-square residual velocity model misfit of less than 2 mm  $\text{yr}^{-1}$  (ref. 11).

The model accounts for recent postseismic vertical motions from the Hector Mine and Landers events, which contribute less than, on average,  $0.2 \text{ mm yr}^{-1}$  of localized uplift and subsidence at the ends of each rupture.

Traditionally, this model has been used to investigate 1000-year earthquake cycle viscoelastic deformation of the San Andreas Fault System (SAFS)<sup>6,8,10</sup>. For a purely elastic model, deep interseismic slip below a locked fault produces narrow regions of uplift along compressional bends and subsidence along tensile regimes. This is a known and intuitive result of elastic half-space deformation models<sup>33,49</sup>. For example, large mountain ranges north of Los Angeles are recognized to be a result of compressional uplift along the Big Bend of the SAFS. To obtain this same physical behaviour using a viscoelastic layered model that includes the effect of gravity, however, requires an omission of east–west-directed body forces that comprise the deep interseismic slip (below the locking depth) mode of the model. When the SAFS is projected into a pole-of-deformation model space<sup>50</sup> (which aligns the fault system in a predominantly north–south direction), only regions with large deviations in orientation from north are impacted by this technique, such as the Big Bend. The end result is a realistic near-field uplifting zone along the Big Bend that simulates geologic uplift in this compressive region<sup>6,8,33</sup>, in addition to a far-field quadrant pattern of alternating uplift and subsidence zones due to earthquake cycle interactions of adjacent fault segments. Geodetic data, however, largely report motions occurring over earthquake cycle timescales (tens to hundreds of years), not necessarily motions occurring on geologic timescales (over thousands of years), as is evident from the lack of strong uplift (and noticeable subsidence) present in the PBO data straddling the Big Bend of the SAFS. To significantly improve our modelling fit in this region, and to ultimately focus our analysis to deformation expected over realistic earthquake cycle timescales, we restored the deep-seated east–west body forces that act below the locking depth of the fault system. This resulting viscoelastic vertical deformation field yields a dominant far-field quadrant pattern of uplift and subsidence with no localized near-field uplift along the Big Bend, in strong agreement with modern GPS observations.

**Code availability.** The source code and documentation for the 3D Fourier Elastic and Viscoelastic Deformation numerical model used in this study to generate the physical model vertical velocity field can be accessed online at [http://topex.ucsd.edu/body\\_force](http://topex.ucsd.edu/body_force).

**Data availability.** The Plate Boundary Observatory GPS vertical velocities used to generate the statistical model vertical velocity field are made publicly available by UNAVCO online at <http://pbo.unavco.org/data/gps>.

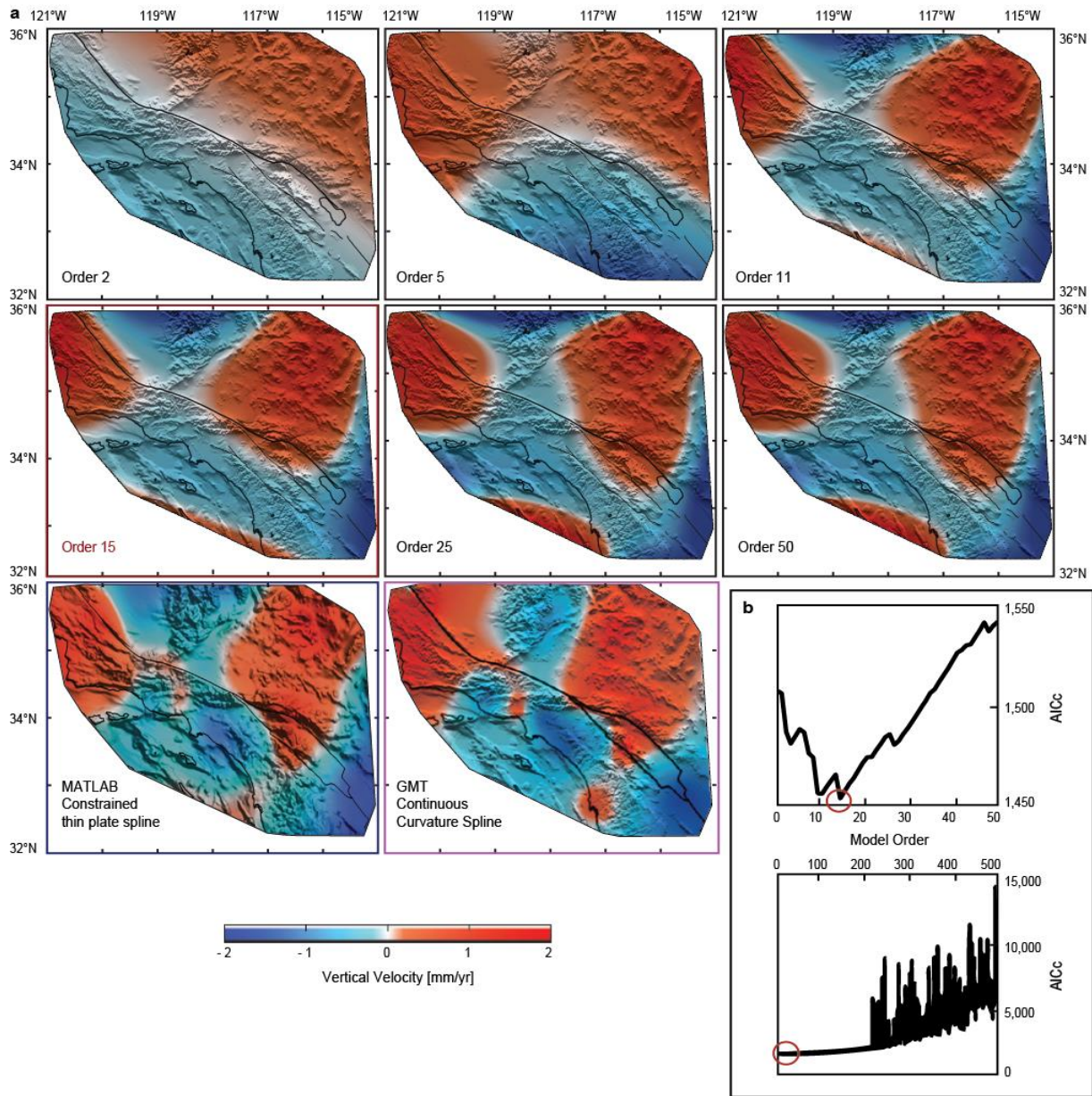
## References

- Akaike, H. A new look at the statistical model identification. *IEEE Trans Automat. Control* **19**, 716–723 (1974).
- Gelman, A. *et al.* *Bayesian Data Analysis* 3rd edn, 356–360 (Chapman and Hall/CRC, 2014).
- Steketee, J. A. On Volterra's dislocations in a semi-infinite elastic medium. *Can. J. Phys.* **36**, 192–205 (1958).
- Smith, B. & Sandwell, D. Coulomb stress accumulation along the San Andreas Fault System. *J. Geophys. Res.* **108**, 2296 (2003).
- Boussinesq, J. *Application des Potentiels a l'Etude de l'Equilibre et du Mouvement des Solides Elastiques* 508 (Gauthier-Villars, 1885).
- Burmister, D. M. The theory of stresses and displacements in layered systems and applications of the design of airport runways. *Proc. Highway Res. Board* **23**, 126–148 (1943).
- Weertman, J. Continuum distribution of dislocations on faults with finite friction. *Bull. Seismol. Soc. Am.* **54**, 1035–1058 (1964).
- Rundle, J. B. & Jackson, D. D. A three-dimensional viscoelastic model of a strike slip fault. *Geophys. J. R. Astron. Soc.* **49**, 575–591 (1977).
- Fay, N. P. & Humphreys, E. D. Fault slip rates, effects of elastic heterogeneity on geodetic data, and the strength of the lower crust in the Salton Trough region, southern California. *J. Geophys. Res.* **110**, B09401 (2005).
- Pollitz, F. F. Transient rheology of the uppermost mantle beneath the Mojave Desert, California. *Earth Planet. Sci. Lett.* **215**, 89–104 (2003).
- Pollitz, F. F. Transient rheology of the upper mantle beneath central Alaska inferred from the crustal velocity field following the 2002 Denali earthquake. *J. Geophys. Res.* **110**, B08407 (2005).
- Hearn, E. H., McClusky, S., Ergintav, S. & Reilinger, R. E. Izmit earthquake postseismic deformation and dynamics of the North Anatolian Fault Zone. *J. Geophys. Res.* **114**, B08405 (2009).
- Panet, I. *et al.* Upper mantle rheology from GRACE and GPS postseismic deformation after the 2004 Sumatra-Andaman earthquake. *Geochem. Geophys. Geosyst.* **11**, Q06008 (2010).
- 2007 Working Group on California Earthquake Probabilities *The Uniform California Earthquake Rupture Forecast, Version 2 (UCERF)* USGS Open File Report 2007-1437, CGS Special Report 203 (US Geological Survey, 2008).
- Savage, J. C. Equivalent strike–slip earthquake cycles in half-space and lithosphere–asthenosphere earth models. *J. Geophys. Res.* **95**, 4873–4879 (1990).
- Meade, B. J. & Hager, B. H. Viscoelastic deformation for a clustered earthquake cycle. *Geophys. Res. Lett.* **31**, L10610 (2004).
- Savage, J. C. Dislocation pileup as a representation of strain accumulation on a strike–slip fault. *J. Geophys. Res.* **111**, B04405 (2006).
- Richards-Dinger, K. B. & Shearer, P. M. Earthquake locations in southern California obtained using source-specific station terms. *J. Geophys. Res.* **105**, 10939–10960 (2000).
- Smith-Konter, B., Sandwell, D. T. & Shearer, P. Locking depths estimated from geodesy and seismology along the San Andreas Fault System: implications for seismic moment release. *J. Geophys. Res.* **116**, B06401 (2011).
- Williams, C. A. & Richardson, R. M. A rheologically layered three-dimensional model of the San Andreas Fault in central and southern California. *J. Geophys. Res.* **96**, 16597–16623 (1991).
- Wdowinski, S., Smith-Konter, B., Bock, Y. & Sandwell, D. T. Diffuse interseismic deformation across the Pacific–North America plate boundary. *Geology* **35**, 311–314 (2007).

# The vertical fingerprint of earthquake cycle loading in southern California

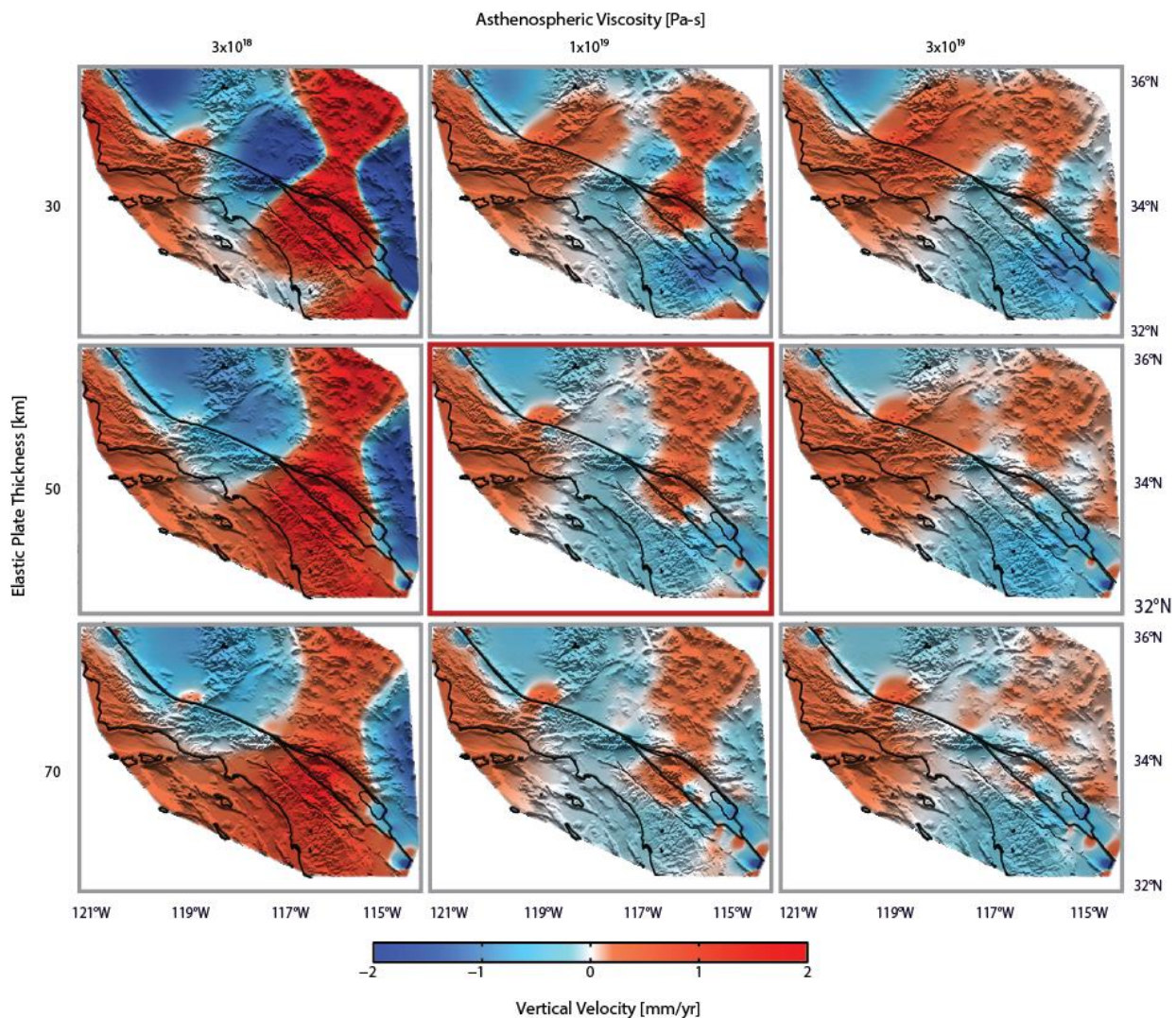
Samuel Howell, Bridget Smith-Konter, Neil Frazer, Xiaopeng Tong and David Sandwell

Extended Data: Vertical fingerprint of earthquake cycle-induced loading of the San Andreas Fault



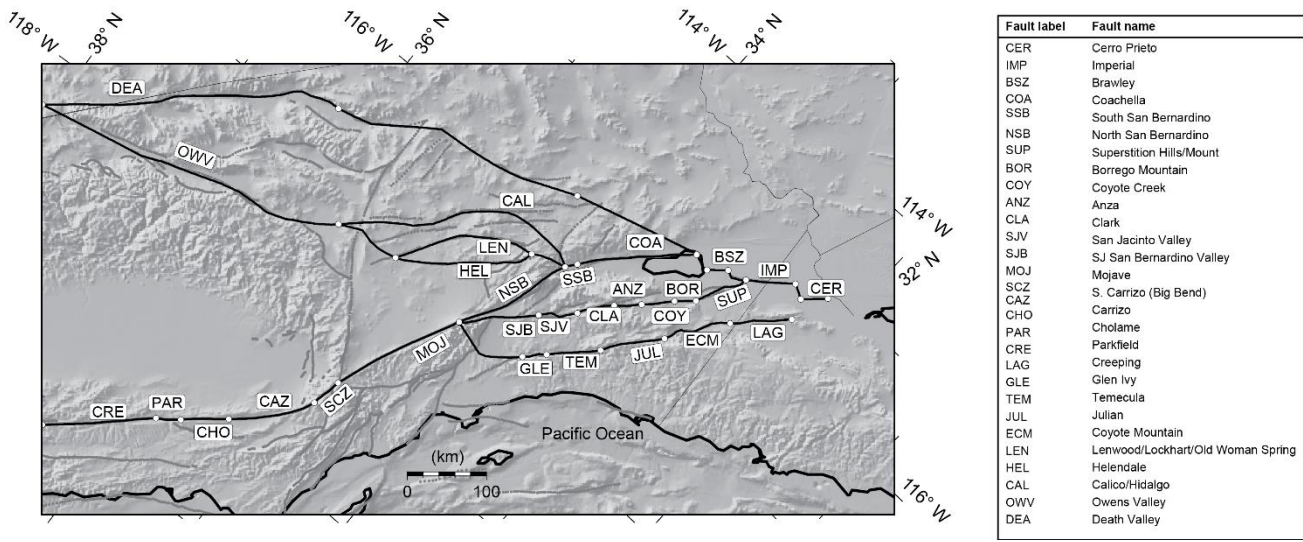
**Extended Data Figure 1 | Statistical modeling results.** (a) Statistical models for different model selection orders (top two rows), with preferred model order 15 highlighted (red box), and splines used for independent verification of results, including a constrained thin plate spline result (blue box) produced with MATLAB’s *tpaps*, and a continuous curvature spline (purple box) produced with GMT’s *greenspline* tool. (b) Sample-size corrected Akaike Information Criterion (AICc) showing a global minimum at model order 15.

## Extended Data: Vertical fingerprint of earthquake cycle-induced loading of the San Andreas Fault



**Extended Data Figure 2 | 3-D earthquake cycle deformation modeling results.** 3D semi-analytic physical models of viscoelastic vertical deformation in response to the past few centuries of earthquake cycle loading (variations in locking depth and historical ruptures). Example models illustrate deformation variations arising from an elastic plate with a thickness of 30-70 km overlaying a viscoelastic asthenosphere with a viscosity of  $3 \times 10^{18} - 3 \times 10^{19}$  Pa-s. The model in the center panel (red outline) minimizes data residuals while maximizing alignment (Extended Data Table 1).

Extended Data: Vertical fingerprint of earthquake cycle-induced loading of the San Andreas Fault



**Extended Data Figure 3 | Schematic of SAFS fault segments used in physical deformation models.** Figure adapted from Tong et al. (2014, with permission), where black lines represent the fault segments used in the physical deformation model, represented by a three-character label. For additional fault model details See Tong et al. (2014). Tong, X., B. Smith-Konter, and D. T. Sandwell (2014), Is there a discrepancy between geological and geodetic slip rates along the San Andreas Fault System?, *J. Geophys. Res. Solid Earth*, 119, doi:10.1002/2013JB010765. ©2014. American Geophysical Union. All Rights Reserved.

Extended Data: Vertical fingerprint of earthquake cycle-induced loading of the San Andreas Fault

**Extended Data Table 1 | Model comparison results.**

Model		Mean	% Alignment
H [km]	$\eta$ [Pa-s]	Residual [mm/yr]	
30	3E+18	1.25	62
30	1E+19	0.52	63
30	3E+19	0.56	60
50	3E+18	0.84	55
<b>50</b>	<b>1E+19</b>	<b>0.44</b>	<b>76</b>
50	3E+19	0.52	66
70	3E+18	0.69	55
70	1E+19	0.48	71
70	3E+19	1.74	64

Mean residual and model alignment between preferred order 15 s-model and each of the 9 tested p-models. Here, alignment is the percent of the study region where the s- and p-models predict the same sense of motion.